THE JOURNAL OF PHYSICAL CHEMISTRY Letters

Letter

Cite This: J. Phys. Chem. Lett. 2019, 10, 5713−5720

pubs.acs.org/JPCL

Crystal Orientation Drives the Interface Physics at Two/Three-Dimensional Hybrid Perovskites

Marine E. F. Bouduban,[†,+] Valentin I. E. Queloz,[‡,+] Valentina M. Caselli,[⊥] Kyung Taek Cho,[‡] Ahmad R. Kirmani,[∥,◇] Sanghyun Paek,[‡] Cristina Roldan-Carmona,[‡] Lee J. Richter,[∥] Jacques E. Moser,[†] Tom J. Savenije,[⊥] Mohammad Khaja Nazeeruddin,[‡] and Giulia Grancini*[,‡,§]

[†]Photochemical Dynamics Group, Institute of Chemical Sciences and Engineering, EPFL, Station 6, CH-1015 Lausanne, Switzerland

[‡]Group for Molecular Engineering of Functional Materials, Institute of Chemical Sciences and Engineering, EPFL, Valais Wallis, Rue de l'Industrie 17, CH-1951 Sion, Switzerland

[⊥]Department of Chemical Engineering, Delft University of Technology, Van der Maasweg 9, 2629 HZ Delft, The Netherlands

[∥]Material Measurement Laboratory, National Institute of Standards and Technology, Gaithersburg, Maryland 20899, United States

Supporting Information

ABSTRACT: Combining halide perovskites with tailored dimensionality into two/three-dimensional (2D/3D) systems has revealed a powerful strategy to boost the performances of perovskite photovoltaics (PVs). Despite recent advances, a clear understanding of the intimate link between interface structure and physics is still missing, leading so far to a blind optimization of the 2D/3D PVs. Here, we reveal the impact of 2D/3D crystal alignment in driving interface charge-recombination dynamics. The 2D crystal growth and orientation are manipulated by specific fluorination of phenethylammonium (PEA), used here as the organic cation backbone of the 2D component. By means of time-resolved optoelectronic analysis from the femto- to microsecond regions, we demonstrate a static function of the 2D layer as an electron barrier and homogeneous surface passivant, together with a dynamic role in retarding back charge recombination. Our results reveal a crucial dependence of such beneficial effects with the 2D layer, leading to an enhanced open-circuit voltage (V_{oc}), mostly attributed to the 2D phase which orients parallel on the 3D layer. Such findings provide a deep understanding and delineate precise guidelines for the smart design of multidimensional perovskite interfaces for advanced PVs and beyond.

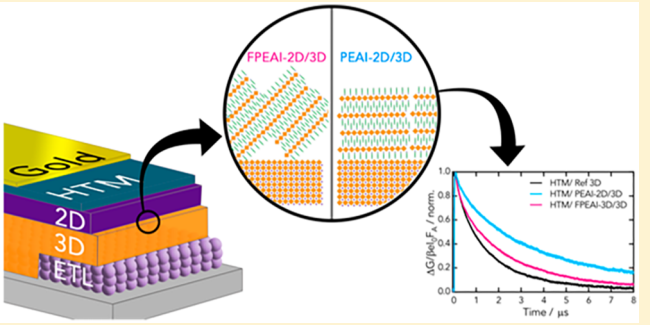

For the last 10 years, three-dimensional (3D) $APbI_3$ halide perovskites (where A is a small organic cation such as methylammonium) have been dominating the scene of next-generation photovoltaics (PVs).[1−3] Their intrinsic hybrid organic−inorganic nature enables great versatility in their structural properties, providing an interesting playground for the design of structures with desirable physical and optoelectronic parameters.[4,5] Cutting the 3D framework along specific crystal planes results in layered systems where the $[PbI_6]$ inorganic slabs are spaced by large organic cations. Among them, Ruddlesden−Popper or "quasi-2D" perovskites, $R_2A_{n-1}Pb_nI_{3n+1}$, with R the organic spacer and n the number of inorganic slabs held together by the small A cation, have recently attracted attention for their key role in addressing the stability issue of perovskite PVs.[6−12] Within this family, if $n = 1$ they form a R_2PbX_4 structure, called hereafter 2D perovskite. $R_2A_{n-1}Pb_nI_{3n+1}$ perovskites thin films exhibit potential for PVs with power conversion efficiency (PCE) around 15%.[13] This limit is mainly dictated by the reduced charge transport with respect to the 3D parent, which is intimately linked with poor control of the crystal growth kinetics and orientation. To encompass this limit, 2D/3D mixed systems have been proposed as efficient and stable solutions,[10,11,14−17] either as 2D/3D blends, where the 2D portion acts as a bulk passivant, or as 2D/3D interface, where the 2D portion functionalizes the perovskite/electron (or hole) transporting layers (ETL/HTM). These mixed solutions have propelled perovskite device performance; however, such empirical evolution of device processing prevents a clear control of the interface properties and structure, leading to a poor "trial and error" device optimization. A solid rationalization of the relation between interface structure and physics is thus urgently needed. For example, how to manipulate crystal growth by material design to drive proper crystallization of the 2D on top of the 3D, or how this impacts the interface charge carrier dynamics in terms of surface trapping, recombination, and device physics are paramount issues to address. Here we consider a stratified nanometer-thick 2D/3D interface based

Received: July 30, 2019
Accepted: September 9, 2019
Published: September 9, 2019

DOI: 10.1021/acs.jpclett.9b02224
J. Phys. Chem. Lett. 2019, 10, 5713−5720

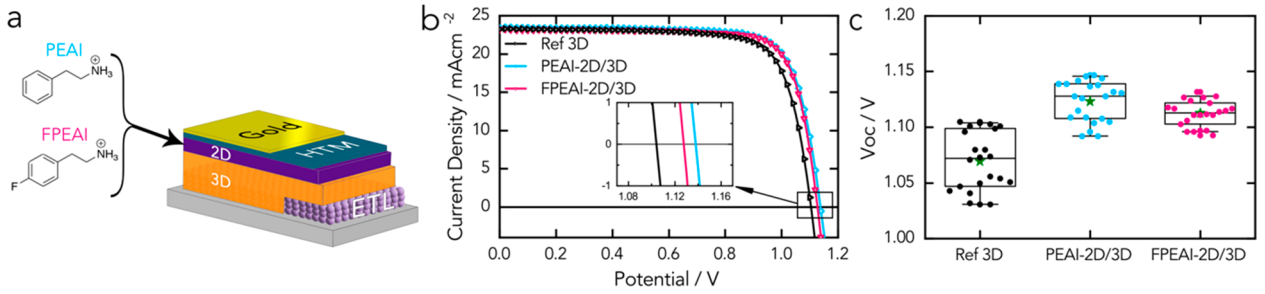

Figure 1. (a) Device stack architecture along with the chemical structure of the two cations used in the 2D layer. (b) Current−voltage characteristic comparing 2D-PEAI/3D, 2D-FPEAI/3D, and ref 3D devices. Inset: zoomed-in portion close to the V_{oc}. (c) V_{oc} statistics (Tukey boxplot) for the two bilayers and the reference cell over 25 devices of each.

on PEA-based 2D/$Cs_{0.1}FA_{0.77}MA_{0.13}PbI_{2.59}Br_{0.41}$ perovskites, where PEAI is phenethylammonium iodide (see Figure 1a), FA formamidinium, and MA methylammonium. When embedded in the device stack (i.e., between the mesoporous oxide ETL and the organic HTM on top), the 2D interface outperforms the standard 3D solar cells, pushing device open-circuit voltage (V_{oc}). We reveal that the beneficial effect of the 2D portion on the device performance is strictly related to the orientation of the crystal planes when growing on top of the 3D portion, as determined by grazing-incidence wide-angle X-ray scattering (GIWAXS) measurements. Importantly, this is dictated by specific fluorination of the cation, resulting in fluorophenethylammonium (FPEA), which affects the crystal orientation of the 2D portion, changing from parallel (with respect to the 3D substrate) to a disordered configuration. In turn, this impacts the interface energetics and subsequent dynamics, which we monitored by combining time-resolved optical spectroscopy from femtosecond to microsecond time scales, together with time-resolved photoconductivity experiments. Our results demonstrate that by modulating the cation either planar or out-of-plane crystal orientation can be achieved. This results in a different interface physics and a more efficient electron barrier and passivation effect for the ordered planar PEAI-based 2D. Embedded in the device, the PEAI-2D functions as a physical spacer between the 3D portion and the HTM, being able to retard charge recombination and ultimately explaining the enhanced V_{oc}. Importantly, the functional interface does not inhibit the current extraction, yielding solar cells with PCE greater than 20%. Our results highlight the importance of properly choosing the 2D organic cation, providing valuable insights toward the exact control and understanding of the 2D/3D structure−function relation, which are paramount for the proper design of efficient multidimensional perovskite interfaces.

Figure 1a presents a sketch of the 2D/3D perovskite solar cell architecture, highlighting the chemical structures of the PEAI and fluorinated analog, FPEAI, obtained by the para-substitution of one fluorine atom on the phenyl moiety cations. Recently, similar compounds have been used in "quasi-2D" based solar cells, showing that the fluorinated version imparts a better alignment of the perovskite sheet stacking, which is responsible for better PCE (around 14%). In our work, we develop a stratified 2D/3D interface where the 2D portion is dynamically grown on top of the 3D portion (see Methods for details). This results in a 2D crust that is a few tens of nanometers thick (20−60 nm, see scanning electron microscopy images in Figure S1).[15,16] Device current−voltage characteristics and parameters are presented in Figure 1b and Table 1, while Figure 1c shows the V_{oc} statistics (see Figure S2 for full device statistics). Solar cells involving a 2D/3D interface outperform their 3D reference, with a clear improvement in the device V_{oc}, without causing a detrimental loss of current. Notably, the boost in the V_{oc} appears higher for the PEAI-based 2D with respect to the FPEAI, overall leading to 20.62% PCE for the champion device. Such improvement asks for a deeper understanding of the optoelectronic processes governing the device operation, which is of key importance for device development and which is often disregarded. The 2D portion being the core of our system, here we investigate the interface processes at the 2D/3D stack as well as at the HTM/2D/3D interfaces making use of a combined series of light-induced spectroscopic tools to shed light on the interface energetics and carrier dynamics on femtosecond to microsecond time scales.

Table 1. Device Parameters for the Champion Solar Cell

	PCE (%)	V_{oc} (V)	J_{sc} (mA cm^{-2})	FF
FPEAI-2D/3D	20.53	1.127	23.21	0.784
PEAI-2D/3D	20.62	1.138	23.43	0.774
ref 3D	19.48	1.104	23.25	0.759

Given the complexity of the 2D/3D system and the paramount importance of the 2D/3D interface energy level alignment, we have combined X-ray photoelectron spectroscopy (XPS) with broadband transient absorption (TA). In TA, the selective excitation of the components will enable the monitoring of the photoinduced processes from 3D → 2D or from 2D → 3D, allowing us to retrieve the energy level alignment. Figures 2a,b displays the TA spectra and dynamics for 3D perovskite and 2D/3D systems upon excitation at λ_{ex} = 600 nm (selectively exciting the 3D), while the plots in Figure 2c,d are obtained upon pumping at λ_{ex} = 390 nm (exciting both 2D and 3D). Exciting only the 3D portion (Figure 2a), the signal is dominated by a large negative feature peaking at 750 nm, which forms with a time constant of 300 fs and persists throughout the investigated time window (1.5 ns). This feature relates to ground-state bleaching (GSB) upon state filling at the 3D perovskite band edge.[17] TA spectra of the 2D/3D systems are identical, with no difference in the evolution of the GSB (Figure 2b). Given that the GSB is proportional to the photoexcited carrier density, its evolution reflects the charge dynamics. Notably, when exciting at λ_{ex} = 390 nm, the TA spectra (Figure 2c) for the 2D/3D differ from the 3D control. Two additional negative features appear in the blue region (500−575 nm). They arise from the direct excitation of the 2D layer and relate to the GSB of the 2D perovskites. Given the spectral position, the peak at 500 nm matches with the GSB from pure R_2PbI_4, while the PB at 550

DOI: 10.1021/acs.jpclett.9b02224
J. Phys. Chem. Lett. 2019, 10, 5713−5720

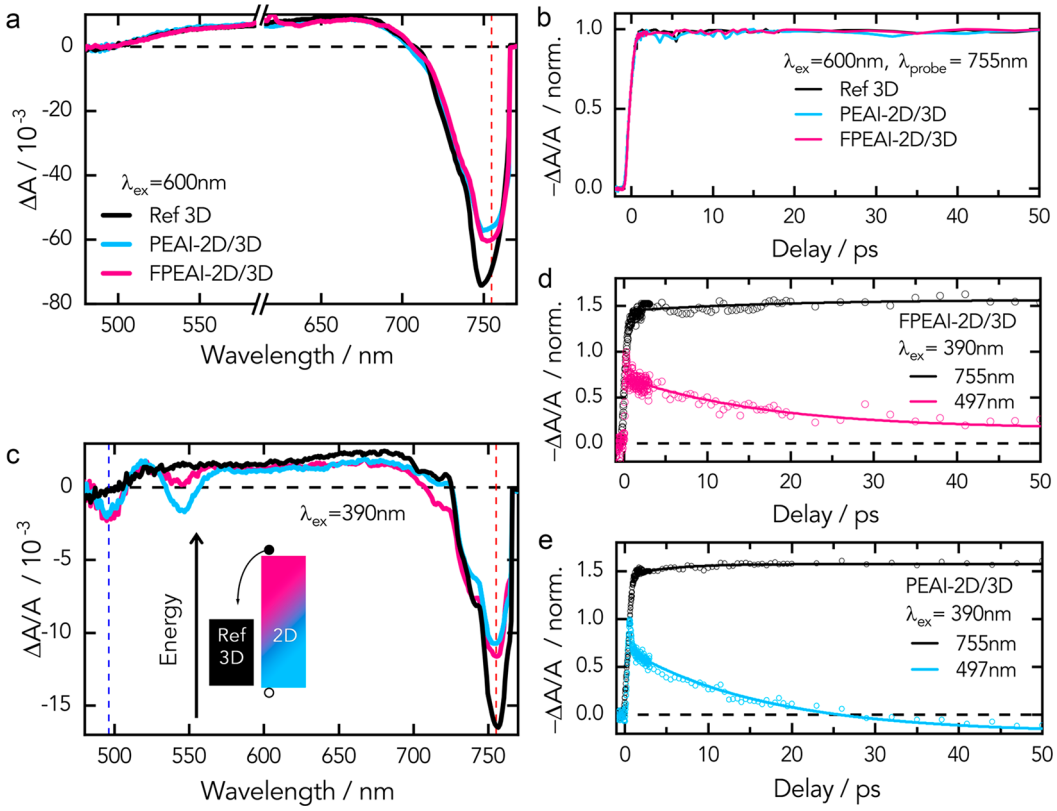

Figure 2. (a) Transient absorption (TA) spectra of 3D perovskite, PEAI-2D/3D, and FPEAI-2D/3D bilayers (excitation wavelength λ_{ex} = 600 nm, carrier density of 10^{18} cm^{-3}) at 1 ps delay (spectra up to 1 ns in Figure S3). (b) TA dynamics at 755 nm comparing 3D perovskite with PEAI-2D/3D and FPEAI-2D/3D bilayers (excitation wavelength λ_{ex} = 600 nm, carrier density of 10^{18} cm^{-3}). (c) TA spectra of 3D perovskite, PEAI-2D/3D, and FPEAI-2D/3D bilayers (excitation wavelength λ_{ex} = 390 nm, carrier density of 10^{18} cm^{-3}) at 1 ps delay (spectra up to 1 ns in Figure S4). Inset: illustration of band diagram and of the charge transfer from the 2D to the 3D perovskite. (d, e) TA dynamics of FPEAI-2D/3D and PEAI-2D/3D, respectively, at 497 and 755 nm upon excitation at 390 nm (carrier density of 10^{18} cm^{-3}). Samples have been excited from the 2D side.

nm can be assigned to PB of an interfacial mixed phase (with n > 1, in agreement with the weak emission from a red-shifted band as shown in Figure S5). Corresponding dynamics of FPEAI-2D/3D and PEAI-2D/3D GSB are presented in Figures 2d,e, compared to the GSB dynamics at 750 nm of the 3D portion. A clear trend is observed: the GSB at 750 nm rises (with a time constant of a few picoseconds, see Table S2) while the GSB at 500 nm decays with a similar time constant. This can be explained as charge or energy transfer from the 2D to the 3D portions. However, we can safely exclude the later upon analysis of the photoluminescence excitation (PLE) map (Figure S6). If energy transfer would have occurred, one would have expected an increase in the PL of the 3D phase, upon excitation in the spectral region where the 2D portion absorbs. In contrast, we observe rather a reduction of the 3D PL signal, indicative of a filtering effect induced by the 2D layer.

Combing this information with the dynamical picture retrieved from the TA analysis, we can thus conclude that electron dissociation happens from the 2D to 3D perovskites. This is enabled by the favorable energy level interface matching, as shown by XPS data on the energy band alignment in Figure S8. The valence band maximum (VBM) of the 2D perovskite is just slightly down shifted by 0.1 eV with respect to the VBM of the 3D perovskite. Given the band gap of 2D perovskites around 3 eV, their conduction band minimum (CBM) lies well above the CBM of the 3D perovskite.[15] This energetically enables electron transfer from the 2D to the 3D portions as indicated by the TA results. The energy level landscape of the 2D/3D system is schematically depicted in the cartoon in the inset of Figure 2c. To gain insight on the free carrier dynamics at the interfaces, a main goal of our work, we employ time-resolved photoluminescence (TRPL) and time-resolved photoconductance (TRPC) measurements targeting the 2D/3D interfaces (Figure 3a,b) as well as the 3D/2D/HTL system (Figure 3c,d). Figure 3a shows the TRPL decays at 780 nm, monitoring the 3D emission with or without the 2D layer. Note that in both cases we selectively excite the 3D portion with an excitation density of 10^{14} carriers/cm.[3] Decays of 3D and FPEAI-2D/3D perovskite show a similar behavior (slightly slower for the FPEAI-2D/3D), while the PEAI-2D exhibits a much slower PL decay (see Table S3 for time constants). Figure 3b shows the TRPC signal, which monitors the free charges generated within the 3D slab and their dynamical evolution (see Figure S9 for carrier density-dependent dynamics). Notably, the initial amplitude of the TRPC signal is proportional to both the yield of free charges generated upon photoexcitation and their mobility, while the decay mirrors the charge immobilization or recombination.[18] No sizable differences are observed between the initial TRPC amplitudes of the 3D and the 2D/3D-modified surfaces (see Figure S10). However, their dynamics are different, as PEAI-2D shows a slower decay with respect to the bare 3D, while it is rather similar in the case of the FPEAI-2D. The combined TRPL and TRPC findings can be rationalized as follows: (i) The initial TRPC amplitudes indicate that no significant 3D → 2D hole transfer is taking place, as this would have lowered the

DOI: 10.1021/acs.jpclett.9b02224
J. Phys. Chem. Lett. 2019, 10, 5713−5720

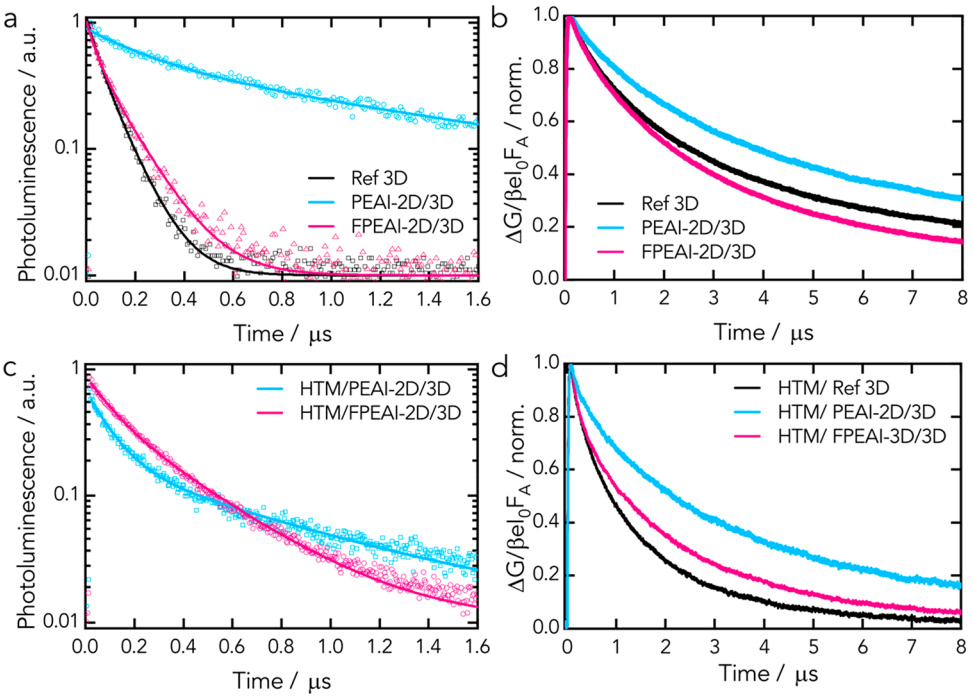

Figure 3. (a) Normalized photoluminescence (PL) decay of PEAI-2D/3D, FPEAI-2D/3D, and ref 3D sample (excitation wavelength λ_{ex} = 635 nm, carrier density of 10^{14} cm^{-3}). (b) Normalized time-resolved photoconductance (TRPC) of the same samples (λ_{ex} = 650 nm, carrier density of 10^{14} cm^{-3}). (c) Normalized PL decay of HTM/PEAI-2D/3D and HTM/FPEAI-2D/3D samples (λ_{ex} = 635 nm, carrier density of 10^{14} cm^{-3}). (d) Normalized TRPC of bilayers of HTM/PEAI-2D/3D, HTM/FPEAI-2D/3D, and HTM/3D (λ_{ex} = 650 nm, carrier density of 10^{14} cm^{-3}). Samples have been excited from the 3D side.

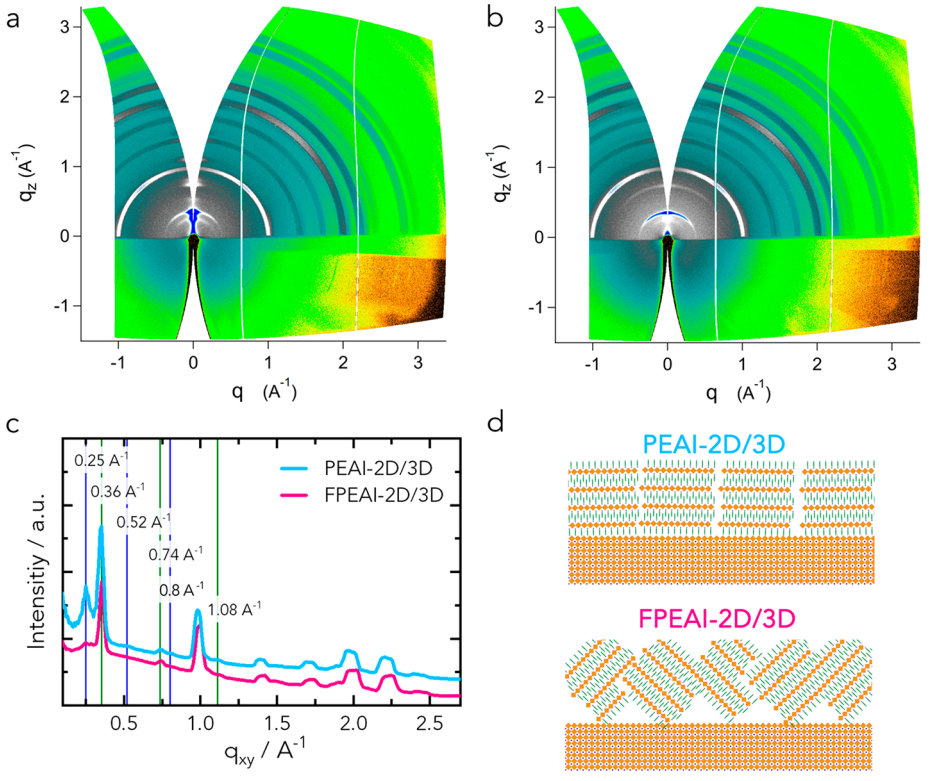

Figure 4. (a) GIWAX map of PEAI-2D/3D showing a parallel preferred orientation in low-q region below the 3D bulk perovskite peak of $q_z = q_{xy}$ = 1.0 $Å^{-1}$. (b) GIWAX map of FPEAI-2D/3D showing more random orientation. (c) 2D GIWAXS sector average for PEAI-2D and FPEAI-2D layers atop 3D bulk. The 2D (n = 1) features are noted by green lines, while the n > 1 (n = 2) features are noted by the blue lines. The PEAI-2D layer clearly shows relatively more intermixing of lower dimensionalities compared to the FPEAI-2D. (d) Cartoon representing preferred orientation of the 2D on top of the 3D bulk.

DOI: 10.1021/acs.jpclett.9b02224
J. Phys. Chem. Lett. 2019, 10, 5713−5720

amplitude of the signal at time zero (for instance, as is the case at the HTM/3D interface, see Figure S10), confirming the TA results. (ii) The slower decay in both PL and TRPC results for PEAI-2D/3D indicates a delayed electron−hole recombination, possibly related to better surface passivation induced by the structural organization and homogeneity of the PEAI-2D layer, as demonstrated in the following (see Table S3). (iii) This does not extend to FPEAI-2D/3D system, which exhibits similar behavior with respect to the bare 3D sample. To determine the kinetic parameters from the TRPC measurements, we have applied the kinetic model described in the Letter by Hutter et al. (see the relevant parameters summarized in Table S5 in the Supporting Information, together with a description of the model and experimental fits in Figure S11).[19] Interestingly, the bimolecular recombination rate constant, k_2, is halved upon addition of PEAI or FPEAI-2D layers on the 3D perovskite. As previously reported, k_2 represents the sum of all bimolecular recombination processes.[20] Therefore, bimolecular recombination processes occurring at the 3D surface are considerably retarded by introducing the 2D perovskite. The enhanced lifetimes in the case of PEAI-2D/3D samples are related to the significantly reduced number of background charges in the material, which slows down the bimolecular recombination. In light of this, and in agreement with the energy level alignment previously discussed, we conclude that the PEAI-2D/3D interface can retard the electron−hole recombination and passivate the 3D surface much more efficiently compared to the FPEAI-based system.

Figure 3c,d shows the TRPL and TRPC signals for 3D/2D/HTM systems. From Figure 3c, the PL shows similar decays, with a slower tail component for the PEAI-2D/3D system (see Table S3 for the time constants). From the TRPC measurements in Figure 3d (see also Figure S10) we can observe that the initial amplitudes drop, and the dynamics get faster if the HTM is deposited on top. This is indicative of a reduction of the charge density due to hole transfers and faster decay due to interfacial recombination. Comparing the TRPC signals of the 3D/HTM with 3D/2D/HTM samples, we observe that the addition of a 2D layer does not hinder the charge transfer to the HTM (initial amplitude reduction, see Figure S10), but recombination is slowed down more visibly for the PEAI-based system. As a physical spacer, holes can be easily delocalized at the 2D/3D interface, given the low energetic barrier perceived by the holes at the 2D phase, thus favoring charge transfer to the HTM. Therefore, the 2D layer can act as a physical spacer where, especially in the case of PEAI-2D, back electron−hole recombination is retarded.

Overall, our results point to a beneficial effect of the 2D layer by reducing surface recombination, which can explain the improvement in the device V_{oc}. As an important remark, we observe that this statement does not hold a general validity but strongly depends on the chemical nature of the organic cation composing the 2D layer. In particular, despite the close energetics and similar electronic structure of their corresponding 2D layers, PEAI-2D/3D and FPEAI-2D/3D behave differently.

To address the reason behind such different behavior, we investigate the structural properties of the interfaces and the crystal plane orientation by GIWAXS measurements. This technique is extremely surface-sensitive at incident angles below the critical angle, allowing one to directly probe the 2D perovskite layer. GIWAXS maps and the corresponding sector averages are shown in Figure 4a,b. Diffraction peaks associated with the lamella structure of the 2D phase are clearly visible for $q < 1.0$ Å^{-1} and correspond to the $(0k0)$ planes. Both the PEAI and FPEAI layers show a major diffraction peak for the pure 2D phase ($n = 1$), with first order at 0.36 Å^{-1} and higher orders at 0.74 Å^{-1} and 1.08 Å^{-1}. We also observe a minor intermixing phase resulting in a weak $n > 1$ ($n = 2$, more precisely) diffraction peak (first order at 0.25 Å^{-1}; higher orders at 0.52 Å^{-1} and 0.80 Å^{-1}). Interestingly, the PEAI-2D layer clearly exhibits the presence of $n > 1$ phase, more visible if compared to FPEAI-2D with a stronger first-order 0.25 Å^{-1} peak. This assignment is also supported by the PL and TA spectra. PL spectra (Figures S3−S5) show a weak shoulder at 550 nm assigned to $n = 2$ quasi-2D perovskite emission; and TA spectra ($\lambda_{ex} = 390$ nm, Figure 2a) exhibit a second peak at 540 nm associated with the GSB of the $n = 2$ quasi-2D perovskite, as previously discussed. The first-order peak at 0.36 Å^{-1} belonging to the $n = 1$ lattice was integrated with respect to the azimuthal angle (χ) to glean information regarding the orientation of the 2D perovskite planes. Results are reported in Figure S12 comparing the FPEAI-2D- and the PEAI-2D-based interfaces. From Figure S12, it is clear that the PEAI-2D peak integral is almost entirely in the range of $\chi = 0°−5°$, suggesting that the layers assume a parallel orientation with respect to the underlying 3D phase and the substrate (as observed in other 2D-based systems).[21] In contrast, the formation of FPEAI-3D layers is more random: a majority of these layers have a 40°−45° orientation with respect to the 3D phase and the substrate (see Figure 4c,d). We suggest that the different crystallite orientation of PEAI-2D and FPEAI-2D is the reason behind the different interfacial physics observed. In the case of the parallel orientation of PEAI-2D, the slowing down of the TRPC dynamics proves that back electron hole recombination (between holes in the HTM and electrons in the 3D perovskite) is retarded, with a direct positive impact on the charge carrier lifetime and thus on the device V_{oc}. The intimate reason behind this lies in the structural orientation of the PEAI-2D and the uniformity of this layer enabling a more perfect homogeneous physical spacer between the 3D perovskite and the HTM. In contrast, the random orientation of FPEAI-2D is responsible for the lack of a beneficial effect of the 2D interlayer in terms of enhanced charge lifetime. In addition, disorder in the 2D portion may allow partial interpenetration of the HTM, leading to behavior of the FPEAI-2D/3D that is similar to that of the 3D-only system. Our findings present a different picture with respect to common knowledge: while much effort has been focused on orienting the 2D planes perpendicular to the substrate in a way to maximize charge transport and extraction,[22−25] here we reveal that, contrarily, planar orientation is needed in the case of 2D/3D interfaces to optimize interface processes and device performances. A similar finding has been revealed for Sn-based 2D/3D interfaces where planar growth of the 2D is essential for device operation.[21] Further analysis, beyond the scope of the presented work, will be needed to clarify the transport mechanism through the organic barrier.

To conclude, we elucidate the optoelectronic properties and carrier dynamics at 2D/3D interfaces leading to highly efficient solar cells. Our results provide compelling evidence of the crucial role of the crystal alignment of the 2D perovskite on top of the 3D perovskite. If the 2D perovskite orients "flat" with respect to the substrate, it can effectively passivate the surface while retarding charge recombination. This results in

DOI: 10.1021/acs.jpclett.9b02224
J. Phys. Chem. Lett. 2019, 10, 5713−5720

an enhanced V_{oc} of the solar cells and overall improved performance. On the other side, a more disordered 2D perovskite alignment limits such beneficial effects. We demonstrate that such alignment can be controlled by fine-tuning the chemical composition of the 2D cation, i.e. by simple atomic substitution, providing a new guideline for material and interface design. Our finding provides a deeper understanding of the main parameters governing the 2D/3D interface physics with important consequences for interface development for solar cells and optoelectronic devices.

METHODS

Device Fabrication and Testing. Fluorine-doped tin oxide (FTO) glass substrates (Nippon sheet glass) were sequentially cleaned with a detergent solution, deionized water, acetone, and ethanol. A compact TiO_2 layer was coated on the cleaned FTO substrate heated at 450 °C by spray pyrolysis deposition. A precursor solution was prepared by diluting titanium diisopropoxide (Sigma-Aldrich) with isopropanol (0.6 mL; 10 mL). Thereafter, we prepared a bilayer electron transport layer with mesoporous TiO_2 and SnO_2. Mesoporous TiO_2 films were prepared using a diluted TiO_2 paste (Dyesol 30 NR-D) solution. Films were prepared by spin-coating and sintered on a hot plate at 500 °C for 30 min. The SnO_2 layer was prepared by spin-coating a precursor solution of $SnCl_4$ (Acros) dissolved in water. A 0.1 M $SnCl_4$ aqueous solution was spin-coated and sintered on a hot plate at 180 °C for 1 h. The lead excess $(FAPbI_3)_{0.85}(MAPbBr_3)_{0.15}$ precursor solution was prepared by mixing FAI (1.1 M), PbI_2 (1.15 M), MABr (0.2 M), and $PbBr_2$ (0.2 M) in a mixed solvent of DMF:DMSO = 4:1 (volume ratio). Another solution of $CsPbI_3$ was also prepared as 1.15 M solution in DMF:DMSO (same volume ratio). For the triple cations mixed perovskite solution, $(FAPbI_3)_{0.85}(MAPbBr_3)_{0.15}$ and $CsPbI_3$ solutions were mixed at a 10:1 vol % ratio. The perovskite precursor solution was spin coated at $33 \times 2\pi$ rad s^{-1} (2000 rpm) for 10 s followed by $83 \times 2\pi$ rad s^{-1} (5000 rpm) for 30 s. Trifluorotoluene (110 μL) was dropped on the spinning substrate at the 10 s point during the second step. The films were annealed at 100 °C for 60 min in a glovebox. For forming an additional 2D perovskite film on top of this perovskite film, substrates were treated with a PEAI (or FPEAI) isopropanol solution. A 100 mL sample of PEAI (or FPEAI) solution (10 mg/mL) was spin-coated on the 3D perovskite films at $83 \times 2\pi$ rad s^{-1} (5000 rpm), which is similar to the antisolvent dropping method. The films were annealed once more at 100 °C for 10 min to make a 2D perovskite layer on the 3D perovskite film. Spiro-OMeTAD was spin-coated at $67 \times 2\pi$ rad s^{-1} (4000 rpm) for 20 s. A 70 mM spiro-OMeTAD solution was prepared by dissolving in chlorobenzene with 4-*tert*-butylpyridine, Li-TFSI in acetonitrile, and $Co[t\text{-BuPyPz}]_3[TFSI]_3$ (FK209) in acetonitrile at a molar ratio of Spiro:FK209:Li-TFSI:TBP of 1:0.03:0.5:3.3. Finally, 70 nm of Au was deposited by thermal evaporation as the back electrode.

The solar cell measurement was done using commercial solar simulators (Oriel, 450 W, Xenon, AAA class). The light intensity was calibrated with a Si reference cell equipped with an IR-cutoff filter (KG3, Newport) and it was recorded before each measurement. Current−voltage characteristics of the cells were obtained by applying an external voltage bias while measuring the current response with a digital source meter (Keithley 2400/2604). The voltage scan rate was 50 mV·s^{-1}, and no device preconditioning such as light soaking or forward voltage bias was applied before starting the measurement. The cells were masked with the active area of 0.16 cm^2 to fix the active area and reduce the influence of the scattered light.

Transient Absorption measurements. Ultrafast transient absorbance (TA) spectra were acquired using femtosecond pump−probe spectroscopy with two different pump wavelengths: λ_{ex} = 390 nm and λ_{ex} = 600 nm. The 390 nm pump beam was obtained by frequency doubling the output of a chirped pulse amplified (CPA) Ti:sapphire laser (CPA-2001, Clark-MXR, 778 nm fundamental central wavelength, 120 fs pulse duration, 1 kHz repetition rate) in a BBO crystal, yielding 200 fs pulses. In turn, the 600 nm excitation beam was generated by directing the CPA output into a noncollinear parametric amplifier (NOPA) and then compressed by a pair of SF_6 prisms, yielding 100 fs pulses. The probe beam was generated by directing a portion of the CPA fundamental output into a CaF_2 crystal, yielding a white light continuum measured over a (400−780) nm spectral domain. The probe fluence at the sample was much lower than that of the pump (39 μJ cm^{-2}). Similarly, the diameter of the probe beam was smaller to ensure homogeneous excitation of the probed area. The dynamics of the photoinduced signals were obtained with a computer-controlled delay-line on the pump path. The probe beam was split before the sample into a beam going through the sample (signal beam) and a reference beam. Both signal and reference beams were directed to respective spectrographs (Princeton Instruments, Spectra Pro 2150i) and detected pulse-to-pulse with 512 × 58 pixel back-thinned charge-coupled-device cameras (Hamamatsu S07030-0906). The pump beam was chopped at half of the laser frequency (500 Hz), and a satisfying signal-to-noise ratio was obtained by typically averaging 3000 spectra. The time resolution of the experiment was 250 fs.

Steady-State Optical Measurement. Steady-state absorption spectra were acquired with a Perkins Elmer lambda 950s ultraviolet/Vis spectrophotometer using an integrating sphere to account for optical losses outside of the active layer.

Steady-state and time-resolved photoluminescence measurement were carried out on a Horiba Fluorolog-3 instrument, with a photomultiplier tube as detector. The excitation source for the TCSPC was a Horiba nanoLED-370 with an excitation wavelength of 369 nm, a pulse duration of 1.3 ns, and a repetition rate of 1 MHz.

Time-Resolved Photoluminescence Measurements. For TRPC measurements the samples have been loaded into airtight resonant cavity (low intensity measurements) and open cell (high intensities) holders in a N_2 filled glovebox. The traces have been measured upon pulsed (10 Hz, 3 ns full-width at half-maximum) photoexcitation at 650 nm from a Q-switched Nd:YAG laser ("Infinity 15-30", Coherent).[26] Excitation intensities have been varied in the range of 10^9−10^{12} photons/cm^2.

GIWAXS Measurements. GIWAXS measurements were carried out in reflection geometry at beamline 7.3.3 of the Advanced Light Source, Lawrence Berkeley National Laboratory. Samples were measured at a detector distance of 0.249 m using an X-ray wavelength of 1.240 Å, at 0.18° angle of incidence with respect to the substrate plane. Calibration was performed with a silver behenate standard. Scattering intensity was detected by a PILATUS 2 M detector.[1] Nika software package was used to sector average the 2D GIWAXS images.[2] Data plotting was done in Igor Pro (Wavemetrics, Inc., Lake Oswego, OR, United States).

DOI: 10.1021/acs.jpclett.9b02224
J. Phys. Chem. Lett. 2019, 10, 5713−5720

■ ASSOCIATED CONTENT

Supporting Information

The Supporting Information is available free of charge on the ACS Publications website at DOI: 10.1021/acs.jpclett.9b02224.

Additional data such as SEM images, device statistics, TA spectra, PLE maps, TRPC decays, and XRD patterns (PDF)

■ AUTHOR INFORMATION

Corresponding Author

*E-mail: giulia.grancini@epfl.ch.

ORCID

Sanghyun Paek: 0000-0002-2671-2909
Lee J. Richter: 0000-0002-9433-3724
Jacques E. Moser: 0000-0003-0747-4666
Tom J. Savenije: 0000-0003-1435-9885
Mohammad Khaja Nazeeruddin: 0000-0001-5955-4786
Giulia Grancini: 0000-0001-8704-4222

Present Address

§(G.G.) Department of Chemistry, Physical Chemistry, University of Pavia, Via Torquato Taramelli 14, 27100 Pavia, Italy.

Author Contributions

+M.E.F.B. and V.I.E.Q. contributed equally to this work.

Notes

The authors declare no competing financial interest.
◇(A.R.K.) Guest researcher.

■ ACKNOWLEDGMENTS

Certain commercial equipment, instruments, or materials are identified in this paper in order to specify the experimental procedure adequately. Such identification is not intended to imply recommendation or endorsement by the National Institute of Standards and Technology, nor is it intended to imply that the materials or equipment identified are necessarily the best available for the purpose. M.E.F.B. gratefully acknowledges financial support by the Swiss National Science Foundation (SNSF) and NCCR MUST, a research instrument of the SNSF. G.G. and V.I.E.Q. acknowledge the Swiss National Science Foundation (SNSF) funding through the Ambizione Energy Project No. 646 HYPER (Grant No. PZENP2173641). Beamline 7.3.3 of the Advanced Light Source is supported by the Director of the Office of Science, Office of Basic Energy Sciences, of the U.S. Department of Energy under Contract No. DE-AC02-05CH11231. We furthermore acknowledge Professor Raffaella Buonsanti for the use of the Fluorolog system for the data reported in Figure 3,a,c.

■ REFERENCES

(1) National Renewable Energy Laboratory (NREL). http://www.nrel.gov/pv/cell-efficiency.html.

(2) Jung, E. H.; Jeon, N. J.; Park, E. Y.; Moon, C. S.; Shin, T. J.; Yang, T.-Y. Y.; Noh, J. H.; Seo, J. Efficient, Stable and Scalable Perovskite Solar Cells Using Poly(3-Hexylthiophene). *Nature* **2019**, *567* (7749), 511−515.

(3) Jiang, Q.; Zhao, Y.; Zhang, X.; Yang, X.; Chen, Y.; Chu, Z.; Ye, Q.; Li, X.; Yin, Z.; You, J. Surface Passivation of Perovskite Film for Efficient Solar Cells. *Nat. Photonics* **2019**, *13* (7), 460−466.

(4) Brenner, T. M.; Egger, D. A.; Rappe, A. M.; Kronik, L.; Hodes, G.; Cahen, D. Are Mobilities in Hybrid Organic-Inorganic Halide Perovskites Actually 'High'? *J. Phys. Chem. Lett.* **2015**, *6*, 4754.

(5) Li, W.; Wang, Z.; Deschler, F.; Gao, S.; Friend, R. H.; Cheetham, A. K. Chemically Diverse and Multifunctional Hybrid Organic-Inorganic Perovskites. *Nat. Rev. Mater.* **2017**, *2* (3), 16099.

(6) Grancini, G.; Nazeeruddin, M. K. Dimensional Tailoring of Hybrid Perovskites for Photovoltaics. *Nat. Rev. Mater.* **2019**, *4* (1), 4−22.

(7) Milot, R. L.; Sutton, R. J.; Eperon, G. E.; Haghighirad, A. A.; Martinez Hardigree, J.; Miranda, L.; Snaith, H. J.; Johnston, M. B.; Herz, L. M. Charge-Carrier Dynamics in 2D Hybrid Metal-Halide Perovskites. *Nano Lett.* **2016**, *16* (11), 7001−7007.

(8) Becker, M. A.; Vaxenburg, R.; Nedelcu, G.; Sercel, P. C.; Shabaev, A.; Mehl, M. J.; Michopoulos, J. G.; Lambrakos, S. G.; Bernstein, N.; Lyons, J. L.; et al. Bright Triplet Excitons in Caesium Lead Halide Perovskites. *Nature* **2018**, *553* (7687), 189−193.

(9) Protesescu, L.; Yakunin, S.; Bodnarchuk, M. I.; Krieg, F.; Caputo, R.; Hendon, C. H.; Yang, R. X.; Walsh, A.; Kovalenko, M. V. Nanocrystals of Cesium Lead Halide Perovskites (CsPbX3, X = Cl, Br, and I): Novel Optoelectronic Materials Showing Bright Emission with Wide Color Gamut. *Nano Lett.* **2015**, *15* (6), 3692−3696.

(10) Even, J.; Pedesseau, L.; Katan, C. Understanding Quantum Confinement of Charge Carriers in Layered 2D Hybrid Perovskites. *ChemPhysChem* **2014**, *15* (17), 3733−3741.

(11) Achtstein, A. W.; Prudnikau, A. V.; Ermolenko, M. V.; Gurinovich, L. I.; Gaponenko, S. V.; Woggon, U.; Baranov, A. V.; Leonov, M. Y.; Rukhlenko, I. D.; Fedorov, A. V.; et al. Electroabsorption by 0D, 1D, and 2D Nanocrystals: A Comparative Study of CdSe Colloidal Quantum Dots, Nanorods, and Nanoplatelets. *ACS Nano* **2014**, *8* (8), 7678−7686.

(12) Chen, Y.; Sun, Y.; Peng, J.; Tang, J.; Zheng, K.; Liang, Z. 2D Ruddlesden−Popper Perovskites for Optoelectronics. *Adv. Mater.* **2018**, *30* (2), 1703487.

(13) Lai, H.; Kan, B.; Liu, T.; Zheng, N.; Xie, Z.; Zhou, T.; Wan, X.; Zhang, X.; Liu, Y.; Chen, Y. Two-Dimensional Ruddlesden−Popper Perovskite with Nanorod-like Morphology for Solar Cells with Efficiency Exceeding 15%. *J. Am. Chem. Soc.* **2018**, *140* (37), 11639−11646.

(14) Chen, Y.; Sun, Y.; Peng, J.; Tang, J.; Zheng, K.; Liang, Z. 2D Ruddlesden−Popper Perovskites for Optoelectronics. *Adv. Mater.* **2018**, *30*, 1703487.

(15) Cho, K. T.; Grancini, G.; Lee, Y.; Oveisi, E.; Ryu, J.; Almora, O.; Tschumi, M.; Schouwink, P. A.; Seo, G.; Heo, S.; et al. Selective Growth of Layered Perovskites for Stable and Efficient Photovoltaics. *Energy Environ. Sci.* **2018**, *11* (4), 952−959.

(16) Cho, K. T.; Zhang, Y.; Orlandi, S.; Cavazzini, M.; Zimmermann, I.; Lesch, A.; Tabet, N.; Pozzi, G.; Grancini, G.; Nazeeruddin, M. K. Water-Repellent Low-Dimensional Fluorous Perovskite as Interfacial Coating for 20% Efficient Solar Cells. *Nano Lett.* **2018**, *18* (9), 5467−5474.

(17) Grancini, G.; Srimath Kandada, A. R.; Frost, J. M.; Barker, A. J.; De Bastiani, M.; Gandini, M.; Marras, S.; Lanzani, G.; Walsh, A.; Petrozza, A. Role of Microstructure in the Electron-Hole Interaction of Hybrid Lead Halide Perovskites. *Nat. Photonics* **2015**, *9*, 695.

(18) Hutter, E. M.; Hofman, J.-J. J.; Petrus, M. L.; Moes, M.; Abellón, R. D.; Docampo, P.; Savenije, T. J. Charge Transfer from Methylammonium Lead Iodide Perovskite to Organic Transport Materials: Efficiencies, Transfer Rates, and Interfacial Recombination. *Adv. Energy Mater.* **2017**, *7* (13), 1602349.

(19) Hutter, E. M.; Eperon, G. E.; Stranks, S. D.; Savenije, T. J. Charge Carriers in Planar and Meso-Structured Organic-Inorganic Perovskites: Mobilities, Lifetimes, and Concentrations of Trap States. *J. Phys. Chem. Lett.* **2015**, *6* (15), 3082−3090.

(20) Brenes, R.; Guo, D.; Osherov, A.; Noel, N. K.; Eames, C.; Hutter, E. M.; Pathak, S. K.; Niroui, F.; Friend, R. H.; Islam, M. S.; et al. Metal Halide Perovskite Polycrystalline Films Exhibiting Properties of Single Crystals. *Joule* **2017**, *1* (1), 155−167.

DOI: 10.1021/acs.jpclett.9b02224
J. Phys. Chem. Lett. 2019, 10, 5713−5720

(21) Shao, S.; Liu, J.; Portale, G.; Fang, H.-H. H.; Blake, G. R.; ten Brink, G. H.; Koster, L. J. A.; Loi, M. A. Highly Reproducible Sn-Based Hybrid Perovskite Solar Cells with 9% Efficiency. *Adv. Energy Mater.* **2018**, *8* (4), 1702019.
(22) Arai, R.; Yoshizawa-Fujita, M.; Takeoka, Y.; Rikukawa, M. Orientation Control of Two-Dimensional Perovskites by Incorporating Carboxylic Acid Moieties. *ACS Omega* **2017**, *2* (5), 2333−2336.
(23) Zhang, X.; Wu, G.; Yang, S.; Fu, W.; Zhang, Z.; Chen, C.; Liu, W.; Yan, J.; Yang, W.; Chen, H. Vertically Oriented 2D Layered Perovskite Solar Cells with Enhanced Efficiency and Good Stability. *Small* **2017**, *13* (33), 1700611.
(24) Chen, A. Z.; Shiu, M.; Ma, J. H.; Alpert, M. R.; Zhang, D.; Foley, B. J.; Smilgies, D. M.; Lee, S. H.; Choi, J. J. Origin of Vertical Orientation in Two-Dimensional Metal Halide Perovskites and Its Effect on Photovoltaic Performance. *Nat. Commun.* **2018**, *9* (1), 1336.
(25) Mao, L.; Stoumpos, C. C.; Kanatzidis, M. G. Two-Dimensional Hybrid Halide Perovskites: Principles and Promises. *J. Am. Chem. Soc.* **2019**, *141* (3), 1171−1190.
(26) Kroeze, J. E.; Savenije, T. J.; Vermeulen, M. J. W.; Warman, J. M. Contactless Determination of the Photoconductivity Action Spectrum, Exciton Diffusion Length, and Charge Separation Efficiency in Polythiophene-Sensitized TiO 2 Bilayers. *J. Phys. Chem. B* **2003**, *107*, 7696−7705.

DOI: 10.1021/acs.jpclett.9b02224
J. Phys. Chem. Lett. 2019, 10, 5713−5720